Supporting Information

Micro-stress pump with variation of stress to boost the ion transport for high-performance sodium-ion batteries

Xin Jin[a], Mengfan Pei[a], Dongming Liu[a], Zihui Song[a], Wanyuan Jiang[a], Runyue Mao[a], Borui Li[a], Xigao Jian[a,b], Fangyuan Hu*[a]

[a] *School of Materials Science and Engineering, State Key Laboratory of Fine Chemicals. Frontiers Science Center for Smart Materials Oriented Chemical Engineering, Technology Innovation Center of High Performance Resin Materials (Liaoning Province), Dalian University of Technology, Dalian 116024, China.*

[b] *State Key Laboratory of Fine Chemicals, Frontiers Science Center for Smart Materials Oriented Chemical Engineering, School of Chemical Engineering, Technology Innovation Center of High Performance Resin Materials (Liaoning Province), Dalian University of Technology, Dalian 116024, China.*

E-mail addresses: hufangyuan@dlut.edu.cn (Fangyuan Hu)

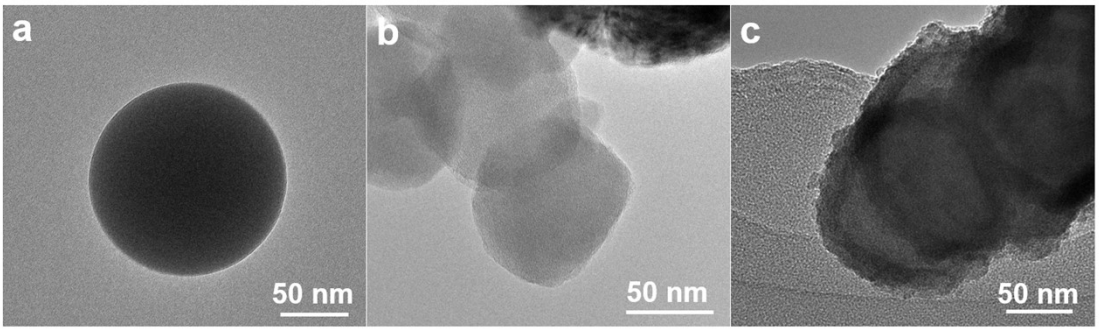

Fig. S1. The high-resolution transmission electron microscopy (HR-TEM) image of (a) liquid metal, (b) carbon sphere and (c) the carbon-coated GaInSn liquid metal nanoparticles (LMNCs).

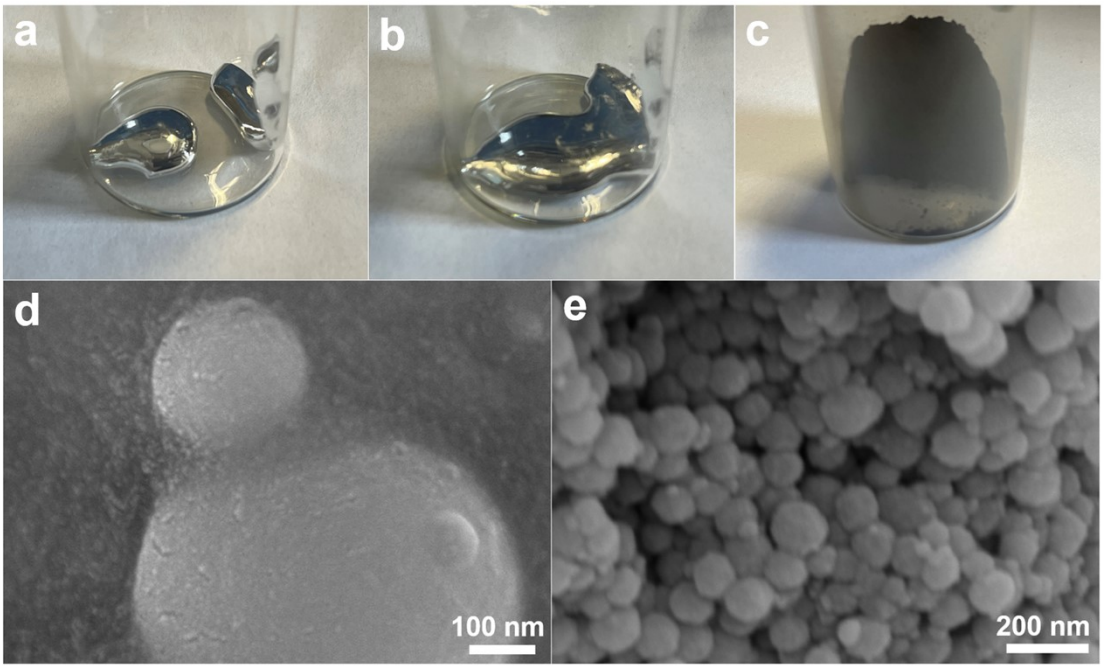

Fig. S2. (a, b) The digital photos of liquid metal. (c) The digital photos of encapsulated liquid metal. SEM images of the (d) LM and (e) LMNCs.

As shown in the Fig. S2, the unique physical properties cause liquid metal to flow significantly, and mutual contaction of liquid metal can affect the whole structure to form a larger unstable spherical structure (Fig. S2a and S2b). Thus, the carbon content is necessary for preventing the aggregation of the liquid metal. In-situ encapsulation of LMNCs avoids agglomeration of the liquid metal and prepares the powder of liquid metal (Fig. S2c). Besides, the SEM image demonstrates that liquid metal particles in contact with each other to form the larger particle, and the structure is unstable (Fig. S2d). Compared the pure liquid metals, the encapsulated particles avoid the aggregation and morphological deformation (Fig. S2e).

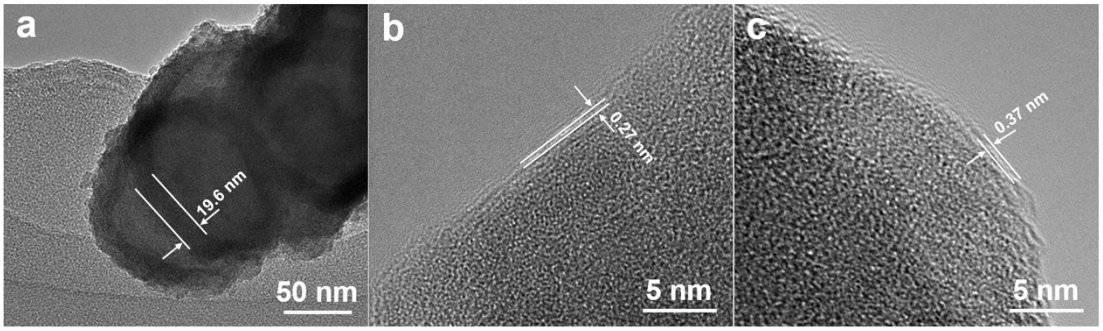

Fig. S3. (a) The TEM images of LMNCs. High-imagination TEM images of (b) NCs and (c)

LMNCs.

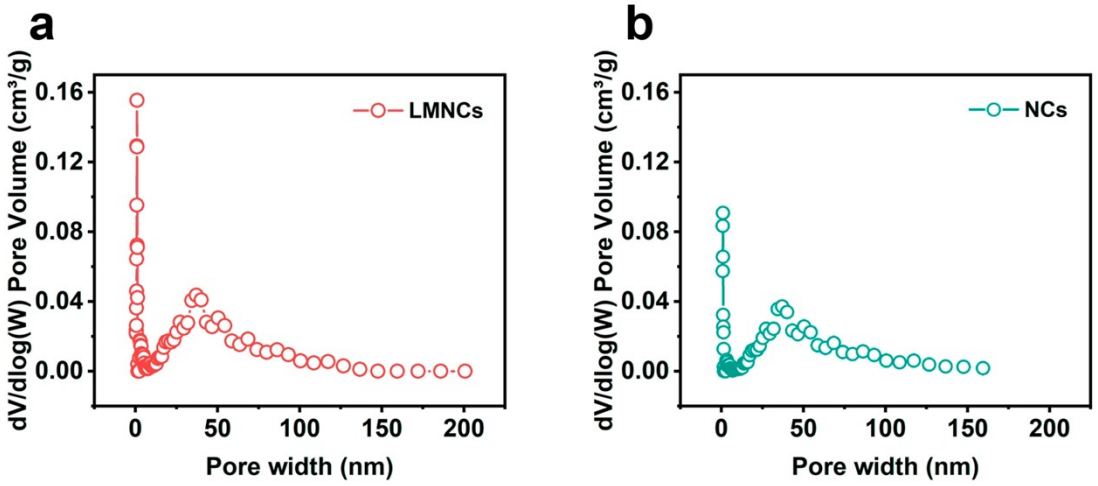

Fig. S4. The analysis of brunauer Emmett teller (BET) in the LMNCs and carbon particles (NCs).

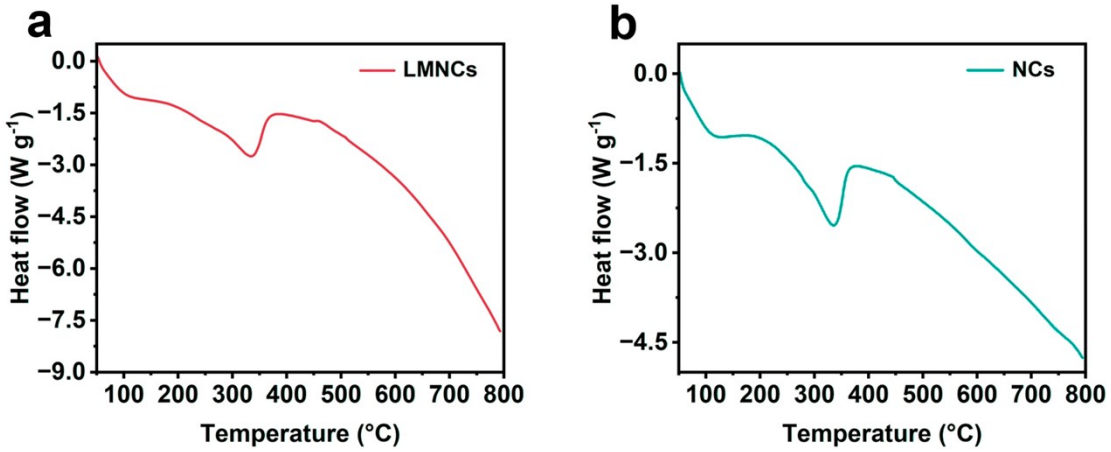

Fig. S5. The analysis of differential scanning calorimetry in the (a) LMNCs and (b) NCs.

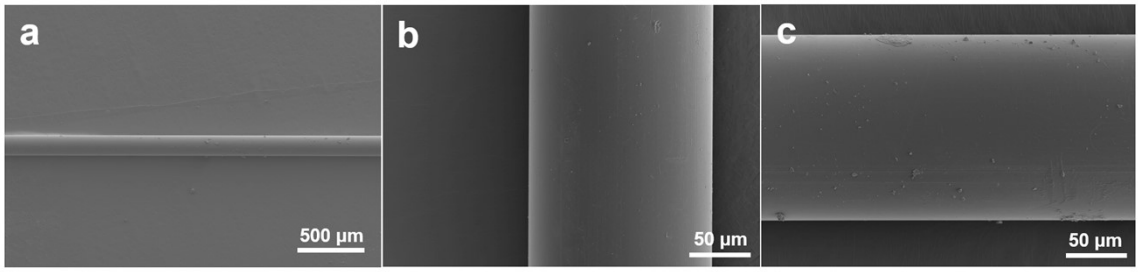

Fig. S6. The SEM images of Fiber Bragg Grating (FBG) from the side view and top view.

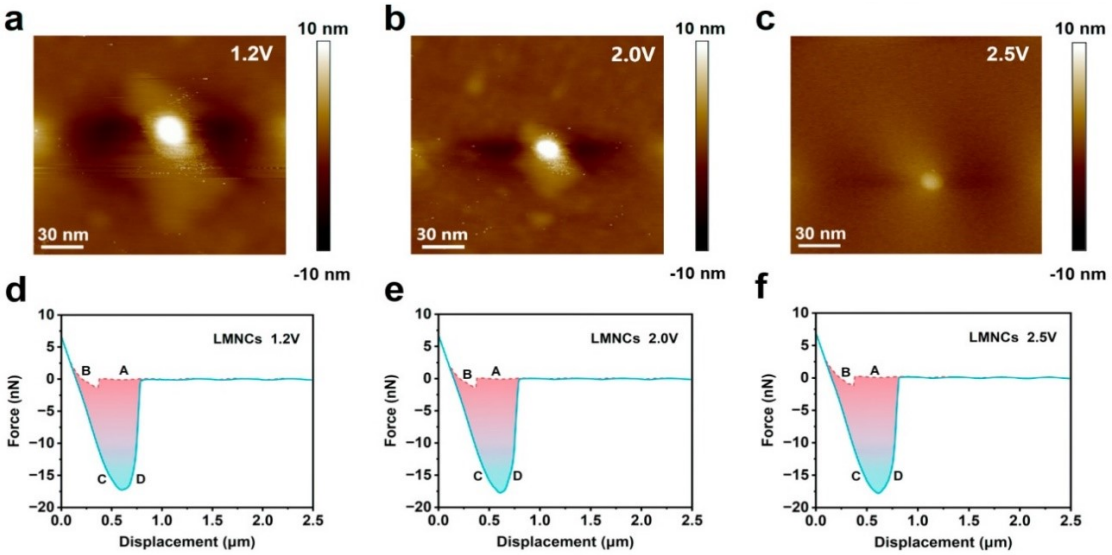

Fig.S7. (a-c) Electrochemical kelvin probe force microscopy (KPFM) of LMNCs of materials at 1.2 V, 2.0 V and 2.5 V. (d-f) Force-displacement curve of LMNCs at 1.2 V, 2.0 V and 2.5 V.

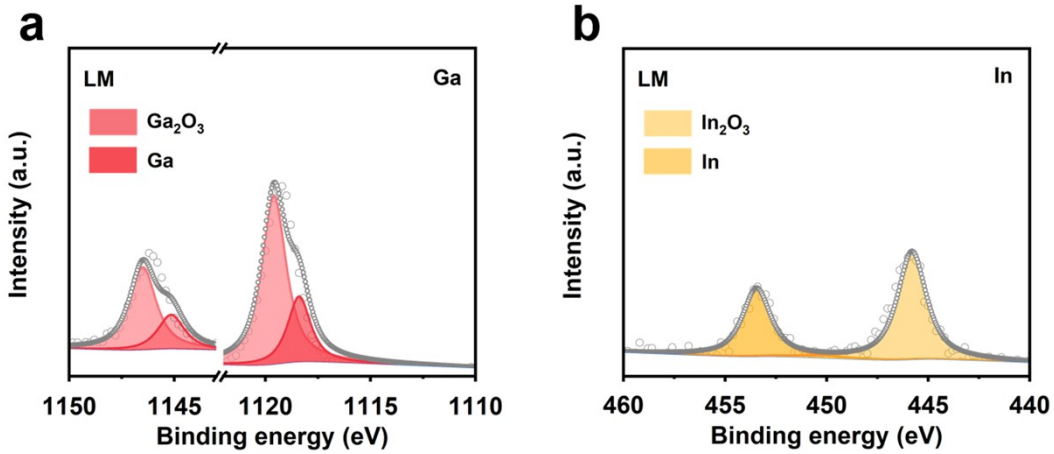

Fig. S8. The X-ray photoelectron spectroscopy (XPS) of LM anode material before cycling.

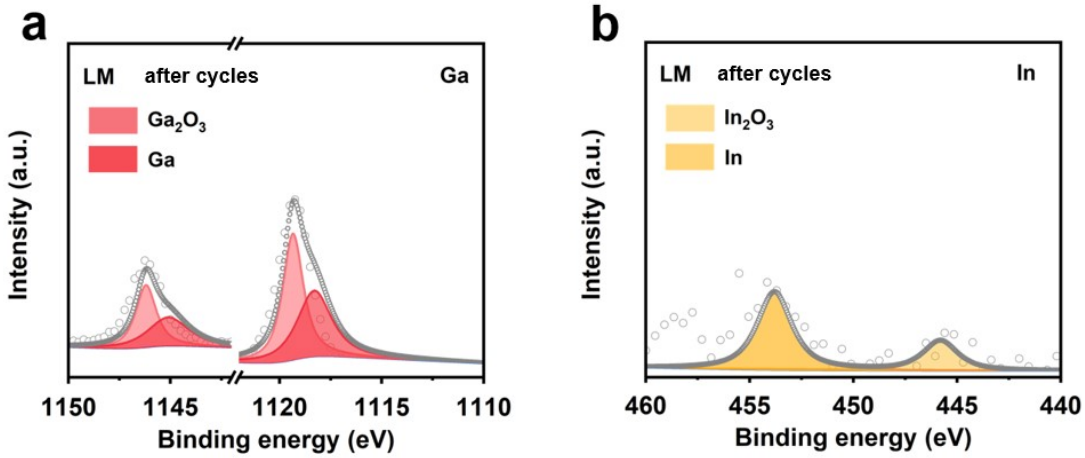

Fig. S9. The X-ray photoelectron spectroscopy (XPS) of LM anode material after cycling.

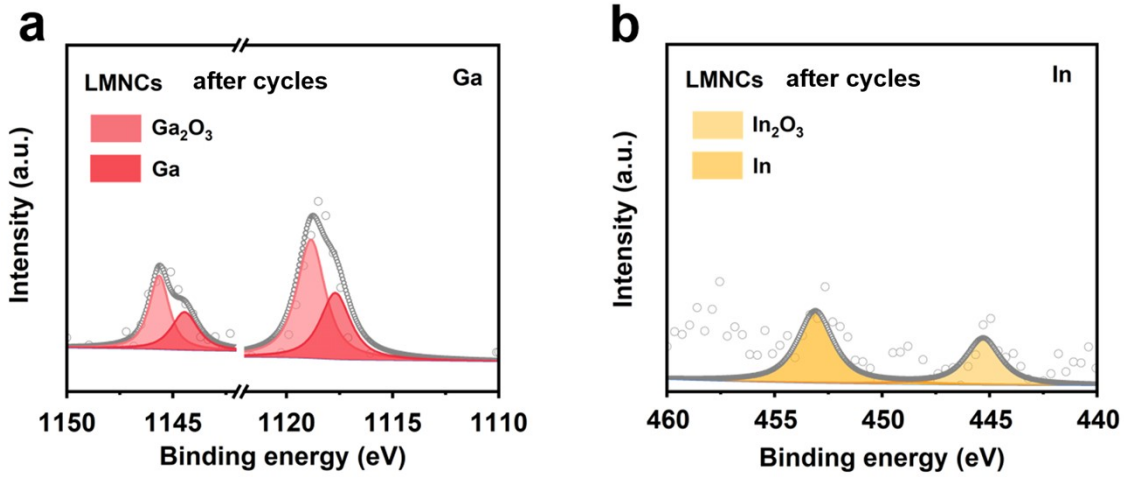

Fig. S10. The X-ray photoelectron spectroscopy (XPS) of LMNCs anode material after cycling.

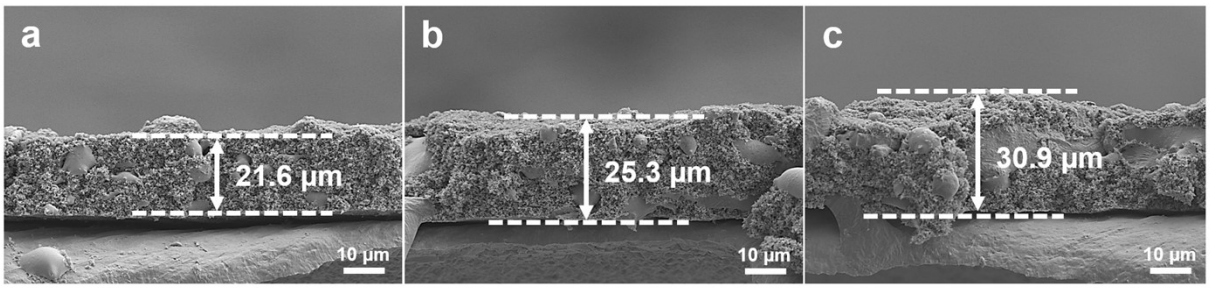

Fig. S11. The cross-sectional SEM images of LM electrode. (a) the original LM anode. (b) the LM anode after 500 cycles. (c) the LM anode after 1500 cycles.

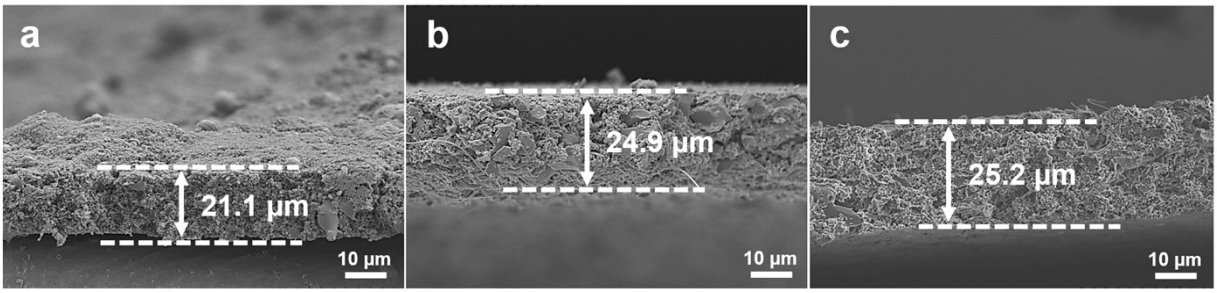

Fig. S12. The cross-sectional SEM images of LMNCs electrode. (a) the original LMNCs anode. (b) the LMNCs anode after 500 cycles. (c) the LMNCs anode after 1500 cycles.

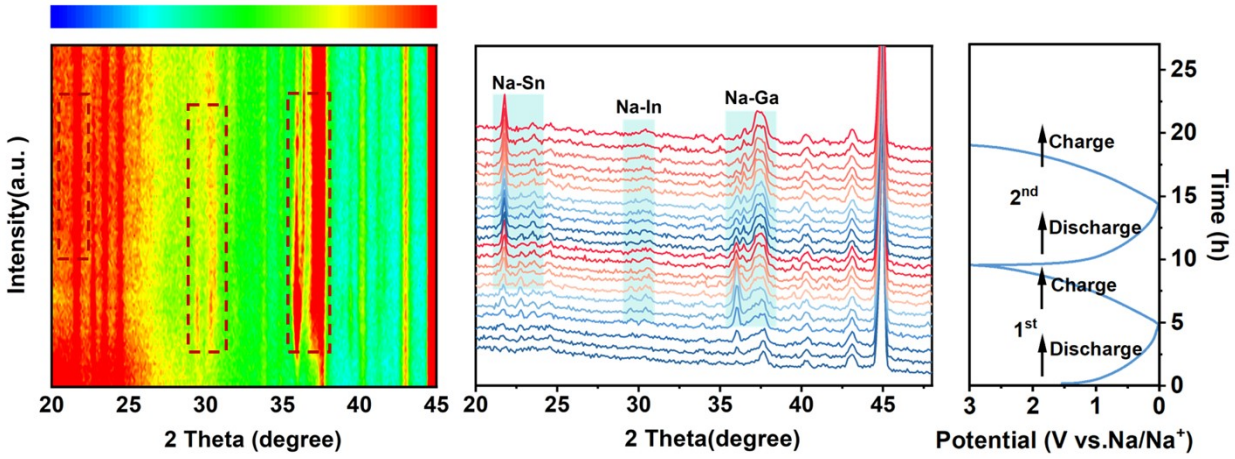

Fig. S13. *In-situ* XRD of the LMNCs electrode with a range of 20°-40° at a current density of 0.1 A g^{-1}, indicating the phase transition and the phase separation during the charging/discharging process.

As the phase transformation exist in the intrinsic Na^+ storage of the liquid metal during the charging/discharging process, we have used the in-situ XRD measurement to analyze the process of sodiation/de-sodiation in the liquid metal-based electrode (Fig. S13). In the beginning of electrochemical reaction, there were no obvious diffraction peaks emerge in the phase transition reaction. We can observe that subsequent diffraction peaks indicate the Sn was preferentially involved in the process of sodiation. In the further sodiation process, Sn was transformed into Na-Sn alloy at 21.7 degree. Besides, the Ga separates from the GaInSn due to the phase transformation, which translates into the Na-Ga alloy, corresponding to the 36 degree. Meanwhile, the new peak occurred at 29.8 degree, corresponding to the formation of Na-In, resulting from the separation of the In due to the alloying reaction of Ga. Then a phase transition from In to sodium alloy emerges in the reaction. The sodiation/de-sodiation reaction are corresponed with the alloying/dealloying

processes, and they devote the capacity to plateau region of the electrode as LMNCs.

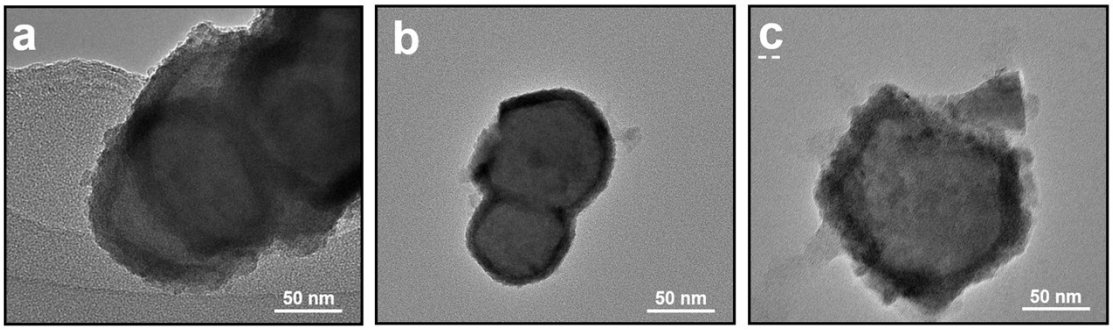

Fig. S14. (a) The TEM images of the LMNCs electrode before cycling. (b) The TEM of electrode was fully discharged and (c) fully charged at 1 A g^{-1}.

The particle size of electrode material is not decrescent, but the structure of LMNCs is different from the initial state. To explore the role of the phase transformation reaction in the excellent electrochemical properties, TEM observation of LMNCs during sodiation/de-sodiation was carried out. The results show the process of sodiation and de-sodiation in the electrode after fully discharged and fully charged at 1 A g^{-1}. The high conductivity and structural integrity of the carbon shell results in the Na^+ transport on the entire surface of the LMNCs, guaranteeing the process of sodiation and de-sodiation to realize the ion transport from the surface to the interior of the LMNCs. In the beginning of sodiation process, Na^+ intercalate into the core of the liquid metal, forming the Na-Ga, Na-In, Na-Sn alloy and the liquid-core structure. With further process, more Na^+ intercalate into the core of liquid metal until LMNCs is completely sodiation.

During sodiation, we can observe that the emergence of some flowing flocs in the LMNCs when Na^+ is extracted, demonstrating that the alloying reaction exists in the Na-based liquid alloy (Fig. S14). Subsequently, the flocs gradually increased as the continuous alloying reaction, and a fluidity color difference appears inside the core-shell structure. And then the color difference disappears as continuous extraction of Na^+. Moreover, the other LMNCs structures were observed after discharge-charge cycle, we can observer the cracked structure with flocculent structure, demonstrating that structural deformation not influence the sodiation and de-sodiation. Therefore, the electrochemical performance is excellent and the rate of redox reaction is guaranteed.

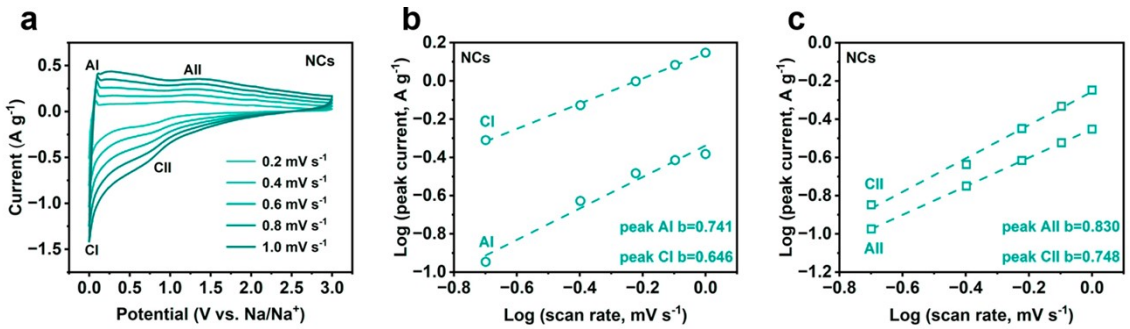

Fig. S15. The electrochemical performance of NCs electrode. a cyclic voltammetry (CV) of NCs electrode. b, c the AI, CI and AII, CII peak current line fitting of NCs electrode.

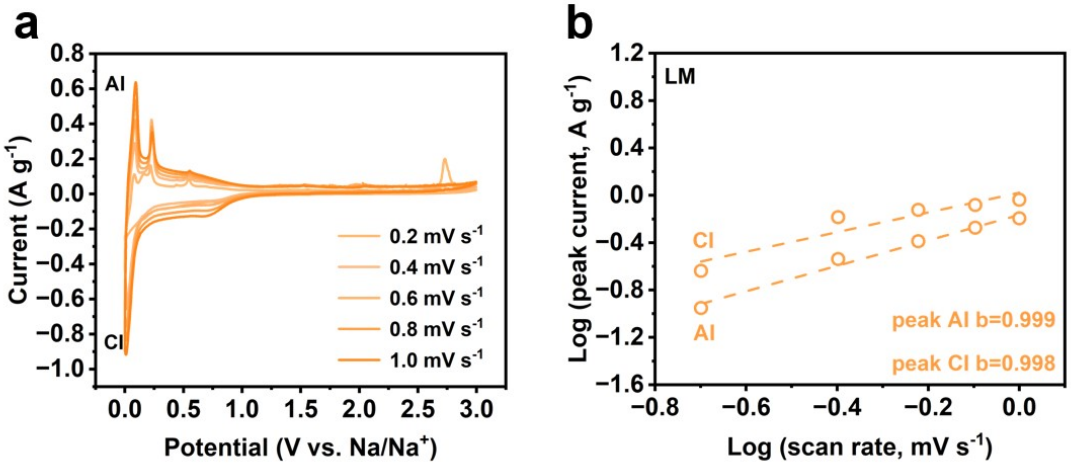

Fig. S16. The electrochemical performance of NCs electrode. (a) cyclic voltammetry (CV) of LM electrode. (b, c) the AI and CI peak current line fitting of LM electrode.

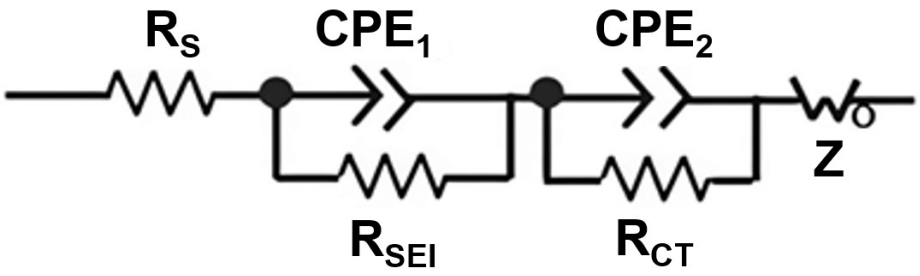

Fig. S17. The corresponding equivalent circuit of EIS test.

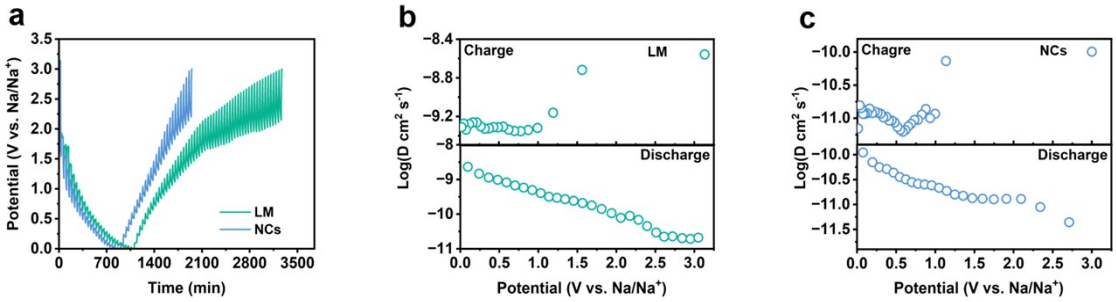

Fig. S18. (a) The result of GITT curves in the NCs and LM. The Na^+ diffusion coefficient in the (b) LM, (c) NCs during charging and discharging process.

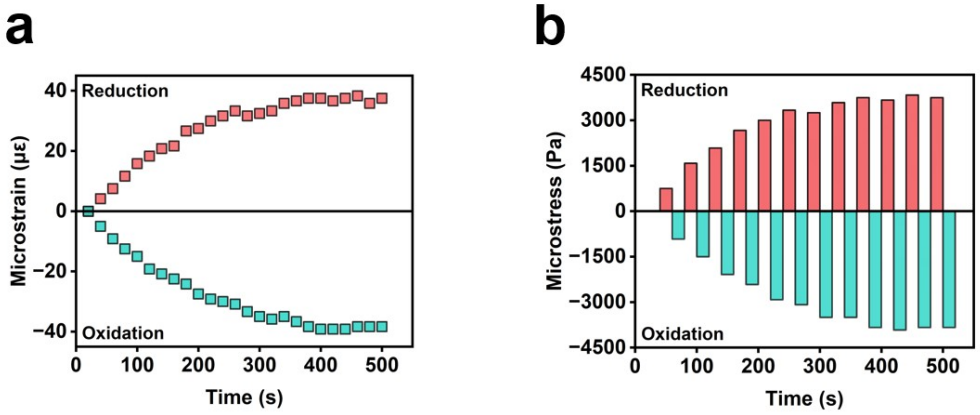

Fig. S19. The schematic of the in-situ micro-stress measurement by Fiber Bragg Grating (FBG).

The in-situ optical fiber sensor technology was applied into the electrolytic cell, and the novel in-situ testing device was designed to reveal the electrochemical mechanism. Fiber Bragg Grating (FBG) was installed on the side of electrode to monitor the change of micro-stress during the redox reaction. This method makes the sensing part and the substrate directly in contact for measurement, achieving the goal of in situ stress monitoring to the utmost extent. Fig 6a. shows that the pressure curve of materials in the electrochemical reaction and value can be calculated. When the voltage increases from 0.01 V to 3.0 V during the oxidation, the wavelength of FBG decreases and inward micro-strain drops gradually. During the process of reduction with the voltage decreases from 3.0 V to 0.01 V, the increasing $\Delta\lambda$ demonstrates that micro-strain rises gradually. The results of measurement show the changes of micro-strain with the changing trend of electrochemical reaction. Micro-stress can be calculated in the Fig. 6b. It is noted that the oxidation behavior becomes more and more obvious, which reduces the inward stress and causes the generation of strain. On the contrary, the reduction behavior boosts the inward stress and promotes the deformation retraction during the reduction process.

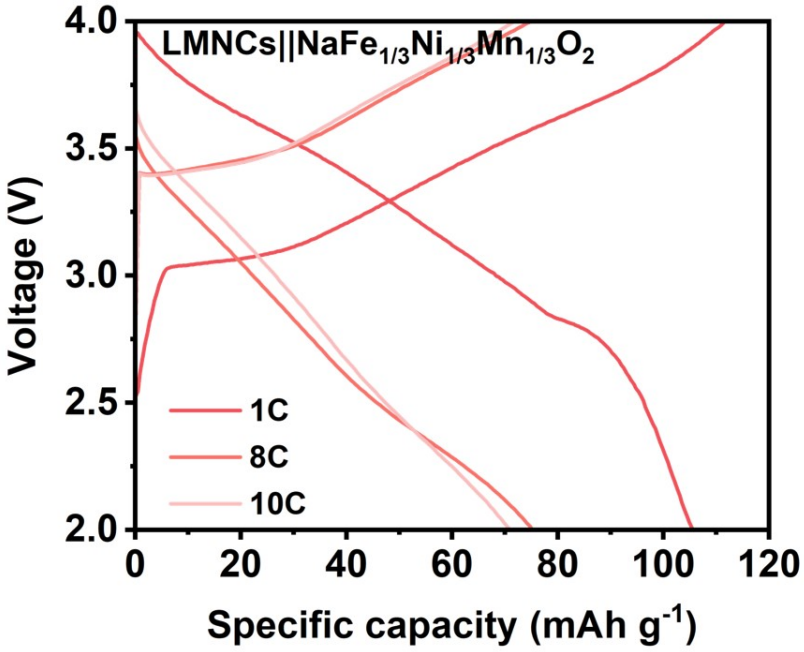

Fig. S20. The first/second/third cycle of discharging/charging curves of materials in the full-cell.

Fig. S21. The photograph from different angles of a winding soft pack cell after electrolyte injecting and sealing.

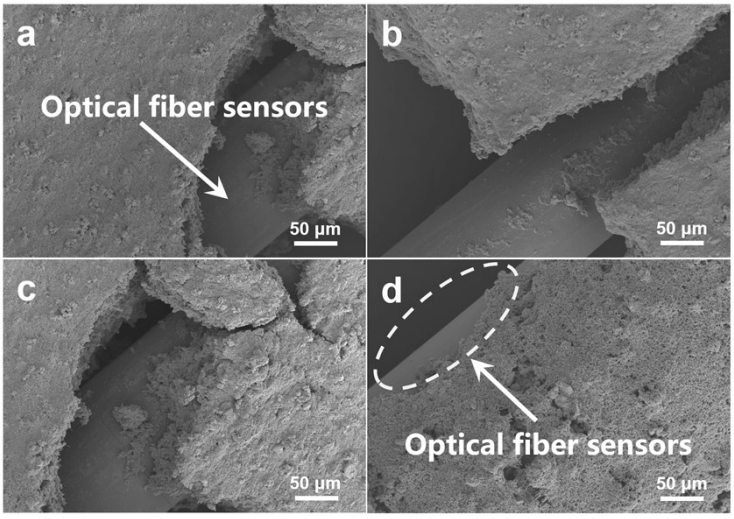

Fig. S22. The close SEM observation of optical fiber sensors was covered by active materials.

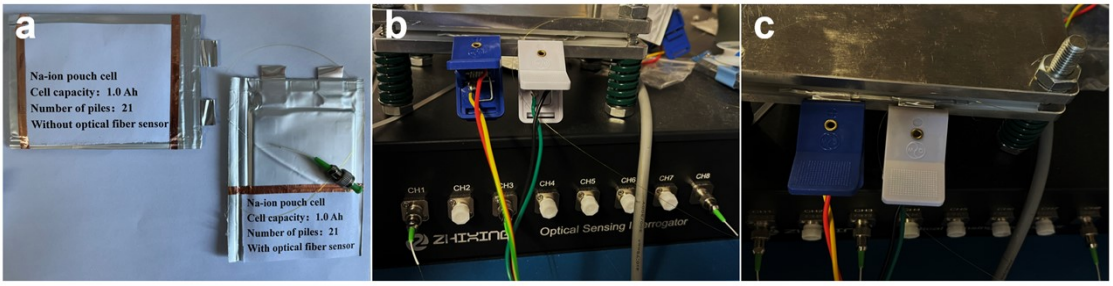

Fig. S23. The cell testing system and the pouch cell was connected to the optical spectrum analyzer.

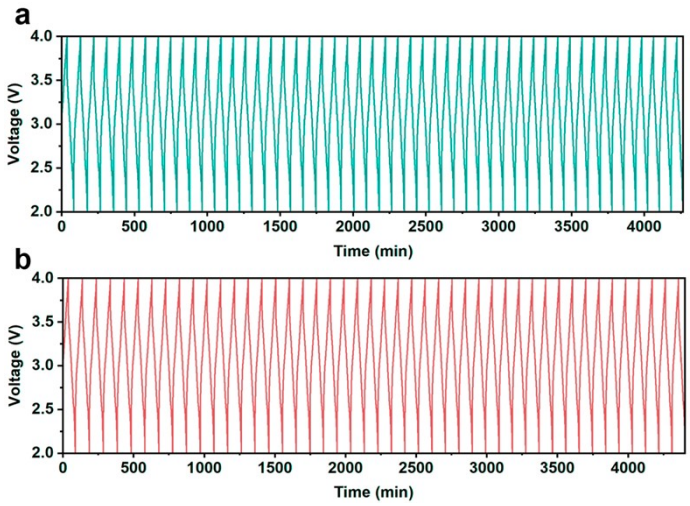

Fig. S24. Comparison of electrochemical characterization of pouch cell. (a) The discharging/charging curve and cycling curve of pouch cells with sensor. (b) The discharging/charging curve and cycling curve of pouch cells without sensor.

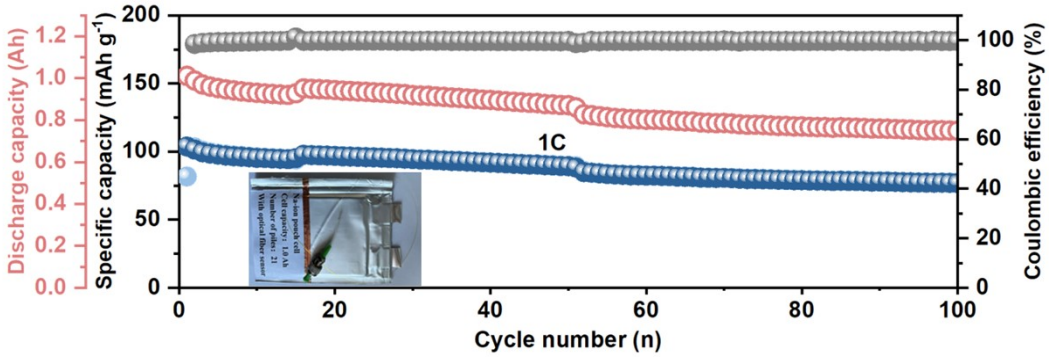

Fig. S25. Electrochemical cycling performance of pouch cell with sensor.

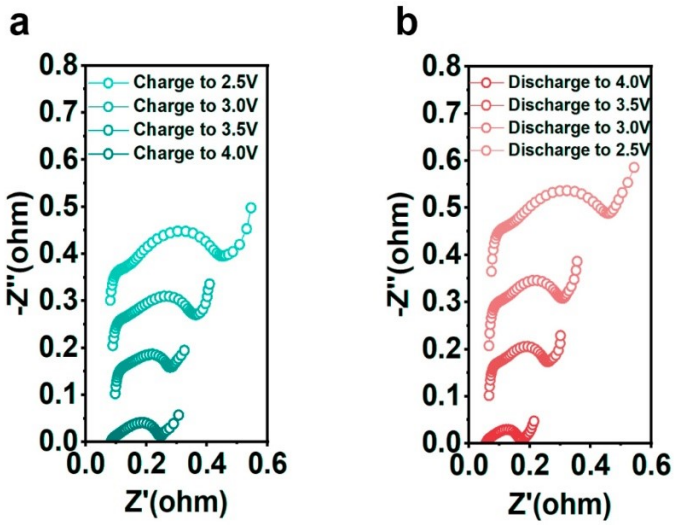

Fig. S26. *In-situ* electrochemical impedance spectra (EIS) of pouch cell with LMNCs anode without sensor.

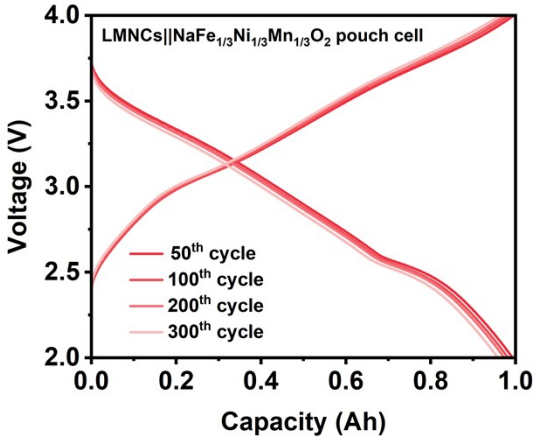

Fig. S27. The galvanostatic charge/discharge curves of different cycles in the LMNCs||$NaFe_{1/3}Ni_{1/3}Mn_{1/3}O_2$ pouch cell.

Table S1. The EIS fitting results of LMNCs in the half-cells at different potential (V vs. Na/Na^+).

Potential (V vs. Na/Na^+)	R_b	R_{SEI}	R_{ct}	State
0.6 V	2.32	11.75	35.25	
0.4 V	2.29	10.23	29.11	Discharg
0.2 V	2.32	8.43	22.19	e
0.01 V	2.33	7.13	18.75	

0.01 V	2.12	7.47	22.05	Charge
0.4 V	2.14	7.84	43.40	
0.8 V	2.14	10.12	57.95	
1.2 V	2.12	12.83	58.29	

Table S2. The EIS fitting results of LM in the half-cells at different potential (V vs. Na/Na^+).

Potential (V vs. Na/Na^+)	R_b	R_{SEI}	R_{ct}	State
0.6 V	1.83	10.28	74.11	Discharge
0.4 V	1.81	8.95	68.83	
0.2 V	1.79	8.42	50.91	
0.01 V	1.79	7.73	37.98	
0.01 V	1.79	7.08	37.98	Charge
0.4 V	1.84	7.28	83.22	
0.8 V	1.85	8.62	87.21	
1.2 V	1.83	9.12	158.21	

Table S3. The EIS fitting results of LMNCs|| $NaFe_{1/3}Ni_{1/3}Mn1_{/3}O_2$ in the half-cells at different potential (V vs. Na/Na^+).

Potential (V vs. Na/Na^+)	R_b	R_{SEI}	R_{ct}	State
3.5 V	3.62	131.23	190.86	Discharge
3.2 V	3.70	143.72	274.84	
2.9 V	3.51	157.99	566.67	
2.6 V	3.67	173.44	832.81	

2.6 V	2.48	143.88	818.25	Charge
2.9 V	2.52	143.66	365.89	
3.2 V	3.13	74.59	221.68	
3.5 V	3.09	63.28	186.86	